Nanoscale

PAPER

View Article Online
View Journal | View Issue

Cite this: *Nanoscale*, 2017, **9**, 3023

Multiscale modeling of plasmonic enhanced energy transfer and cavitation around laser-excited nanoparticles†

Adrien Dagallier,[a] Etienne Boulais,[a,b] Christos Boutopoulos,[a,c] Rémi Lachaine[a] and Michel Meunier*[a]

Received 9th November 2016,
Accepted 1st February 2017

DOI: 10.1039/c6nr08773f

rsc.li/nanoscale

Nanoscale bubbles generated around laser-excited metallic nanoparticles are promising candidates for targeted drug and gene delivery in living cells. The development of new nanomaterials for efficient nanobubble-based therapy is however limited by the lack of reliable computational approaches for the prediction of their size and dynamics, due to the wide range of time and space scales involved. In this work, we present a multiscale modeling framework that segregates the various channels of plasmon de-excitation and energy transfer to describe the generation and dynamics of plasmonic nanobubbles. Detailed comparison with time-resolved shadowgraph imaging and spectroscopy data demonstrates that the bubble size, dynamics, and formation threshold can be quantitatively predicted for various types of nanostructures and irradiation parameters, with an error smaller than the experimental uncertainty. Our model in addition provides crucial physical insights into non-linear interactions in the near-field that should guide the experimental design of nanoplasmonic materials for nanobubble-based applications in nanomedicine.

Introduction

Interaction of light with nanoscale metallic materials may excite collective modes of oscillation of their quasi-free electrons, called surface plasmons, which have been at the origin of spectacular development in the area of nano-optics.[1] This resonant phenomenon enables fast and highly localized energy transfer that allows manipulating matter with unprecedented precision at the nanoscale.[2] Following irradiation with ultrashort laser pulses, rapid heating of the nanoparticle (NP) combined with non-linear photoionization of a nanoplasma[3,4] in the near-field potentially triggers the emission of strong shockwaves and the formation of sub-micron bubbles, whose size and dynamics are finely controlled by the appropriate choice of NP geometry and irradiation parameters.[3,5,6]

These nanobubbles are unique, controllable vessels of thermal and mechanical energy that can daintily interact with materials at the nanoscale. Particularly, they constitute efficient vectors for precisely inducing transient and permanent damage to live cells, stimulating the development of novel approaches to nanoscale surgery,[7,8] cancer therapy[9–11] and cell transfection.[12,13] Appropriate conjugation of the NP surface with functional groups additionally allows selective binding to specific proteins and peptides with high affinity, enabling targeted therapy and drug delivery.[10,14,15]

This objective however remains especially challenging due to the wide range of time (10 fs–100 ns) and space (1 nm–10 μm) scales of the various energy transfer mechanisms involved in the laser-induced cavitation process. Although many theoretical and computational methods have been developed to describe such molecular processes, these are either too computationally intensive or too limited in scope to enable efficient prototyping of the NP geometry or laser parameters for nanomedicine. While full atomistic molecular dynamics methods are the current state-of-the-art for accurate simulation of nanoscale processes, size and speed limitations are prohibitive for these ≃100 ns, ≃10 μm^3, aperiodic systems. Alternative schemes coupling molecular and continuum dynamics, or

[a]*Laser Processing and Plasmonics Laboratory, Department of Engineering Physics, Polytechnique Montréal, Montreal, Quebec, H3C 3A7, Canada.*
E-mail: michel.meunier@polymtl.ca
[b]*Laboratory of Biosensors and Nanomachines, Department of Chemistry, Montreal, Quebec, H3T 1J4, Canada*
[c]*SUPA, School of Physics and Astronomy, University of St. Andrews, North Haugh, St. Andrews, KY16 9SS, UK*

†Electronic supplementary information (ESI) available: Additional details of the modeling framework, including all equations and parameters; precisions on the optimization scheme; values of the experimental cavitation thresholds with their error bars; consideration on the importance of surface effects for small bubbles; details of the numerical reconstitution of the scattering imaging technique signal; additional plasma characterization at the cavitation threshold. See DOI: 10.1039/c6nr08773f

using full continuum hydrodynamic models have been demonstrated to successfully predict the temporal evolution of laser-induced nanobubbles,[3,16,17] but are still too computationally demanding for prototyping. Therefore, the only computational approach currently available consists of extremely simplified models that typically avoid calculating directly the bubble dynamics *via* a plasma-related criterion to estimate the cavitation threshold, which strongly restricts their applicability and accuracy.[6] Finally, many groups have developed modeling frameworks based on Rayleigh–Plesset-like equations that do not model the laser–nanomaterial interaction and whose initial conditions are determined self-consistently from the experimentally obtained maximal bubble diameter;[18–20] they cannot therefore be used as predictive tools.

In this work, we present a new multiscale computational framework that allows for fast, reliable and quantitative prediction of complete bubble dynamics around NPs from first principles. Starting from the laser irradiation parameters and plasmonic NP composition and geometry, we demonstrate that our model accurately predicts the cavitation onset and temporal evolution for a wide range of incident laser fluences (0–400 mJ cm^{-2}), wavelengths (400 nm and 800 nm), pulse widths (45 fs–5 ps), nanoparticle sizes (9–210 nm) and shapes (spherical gold nanoparticles (AuNPs) and gold nanoshells with silica cores (AuNSs)). Comparison with the results from recent literature as well as data coming from our own shadowgraph imaging and time-resolved spectroscopy experiments shows very good agreement with the simulation results. Our multiscale approach segregates the 3D, nanoscale and ultrafast (10 fs–10 ps) energy deposition process from the 0D, microscale and relatively slow cavitation onset and bubble dynamics to enable fast and efficient calculation that, for the first time, makes prototyping plasmonic nanomaterials accessible for nanoscale cavitation and related nanomedicine (Fig. 1).

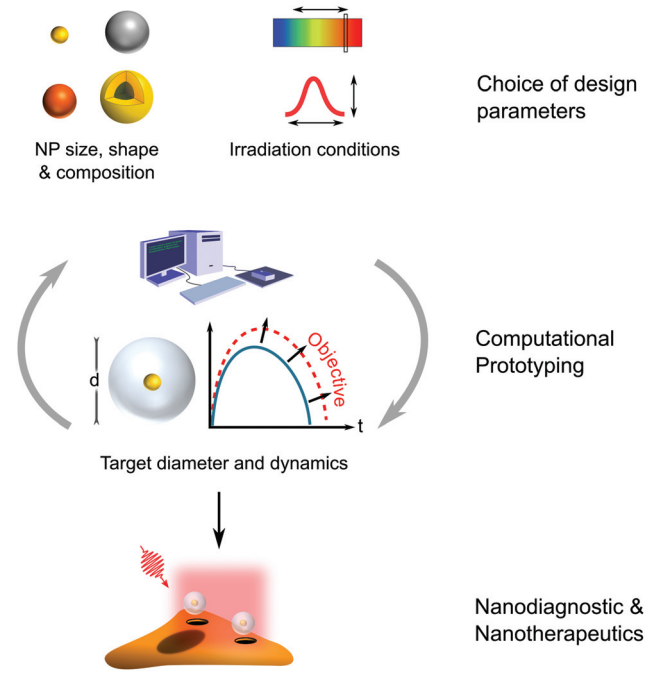

Fig. 1 Design of NPs and irradiation protocols for nanomedicine applications. Numerical optimization of the NP size, shape and composition and of the laser parameters to achieve a given target bubble diameter and temporal evolution makes biological applications possible.

Results and discussion

As illustrated in Fig. 2a, plasmons excited in water-immersed metallic nanoparticles are short-lived and decay in 10–100 fs into hot carriers[21–23] that are ultimately dissipated as heat in the particle and its surrounding through conduction at the metal–water interface.[24] Plasmon excitation additionally concentrates the electromagnetic field in a small volume near the particle[2,25] which, when immersed in water, can lead to the non-linear excitation of a nanoscale plasma in ≃100 fs–5 ps,[4] akin to laser photoionization of pure water.[26] The energy stored in the plasma is transferred to the water molecules in a few picoseconds, leading to high stress and thermal confinement.[27,28] The resulting extreme temperature and pressure induce cavitation in ≃1 ns, leading to the formation, growth and collapse of a bubble that can extend up to a diameter of 0.1–10 μm, with lifetimes of ≃100 ps–100 ns.[19,29,30] Our modeling framework is therefore divided into three distinct sub-models (I. Energy deposition, II. Cavitation, and III. Bubble dynamics) that describe separately the various plasmon decay and energy transfer channels that occur in distinct time scales (Fig. 2b).

The energy deposition sub-model (Sub-Model I) covers the first ≃10 ps and describes the interaction of the electromagnetic field with the nanoparticle, as well as the early thermodynamic evolution of the metal and surrounding water. Here, we are interested in laser pulses shorter than the characteristic molecular collision time (≃10 ps).[3,28] The energy deposition process can therefore be completely isolated from the description of the subsequent cavitation and bubble dynamics. In this sub-model, the plasmon-enhanced electromagnetic field distribution, the NP electron, lattice and water temperatures, the plasma density and kinetic energy density and the total deposited energy are computed in 3D with the finite elements software Comsol (Comsol, Inc., Burlington), following an approach previously developed and validated.[3,16,31] Readers are referred to the Methods section and ESI I† for additional details.

The cavitation sub-model (Sub-Model II) describes the onset of the vapor bubble and the initial shockwave emission that occur in 10–100 ps.[3,26] The initial volume, density, energy, and water–vapor interface velocity after the shockwave emission are determined using the initial water thermodynamic evolution calculated in Sub-Model I. Energy transfer to the water molecules occurs on different time scales, and in physically distinct regions around the particle, depending on whether it originates from the near-field plasma or from heat conduction at the NP–water interface. Since heat conduction

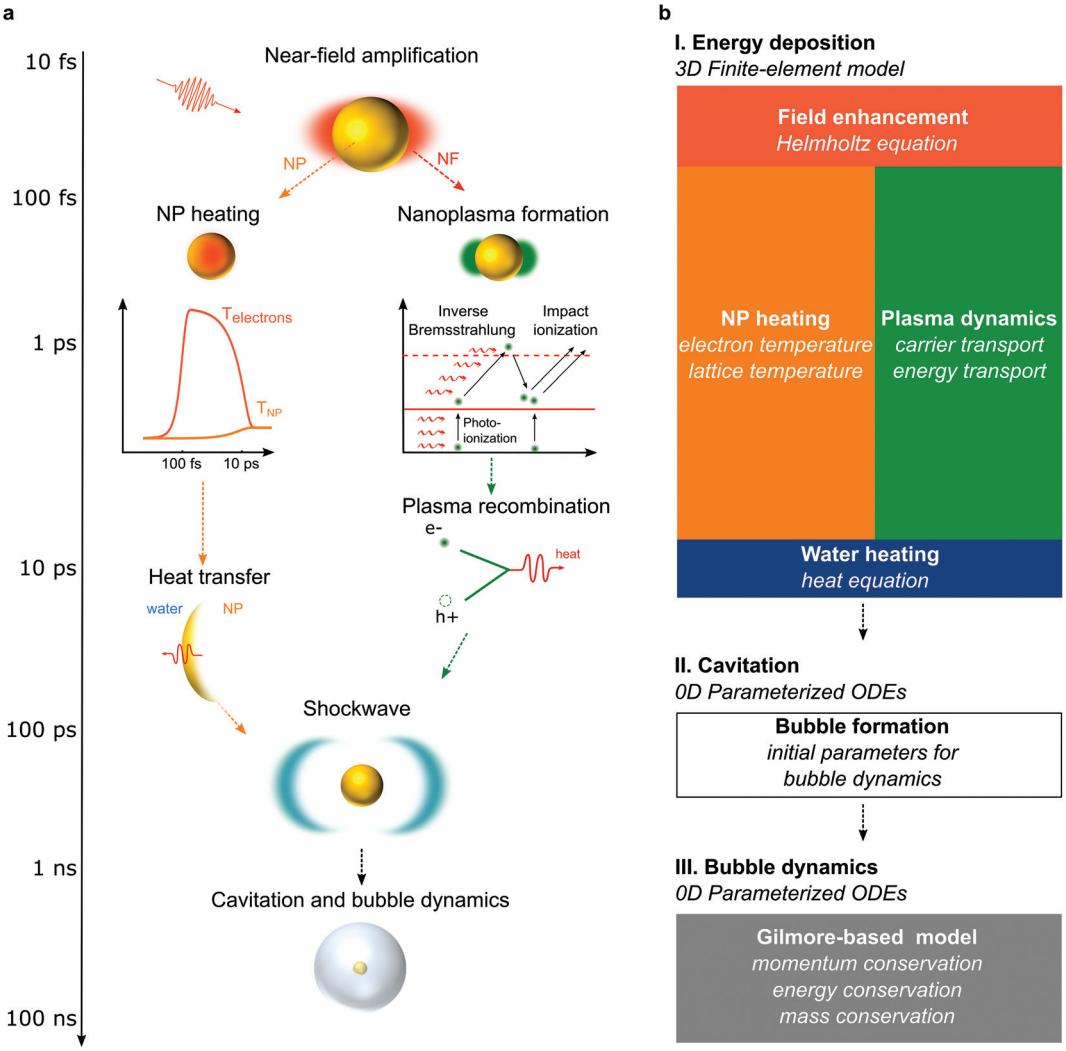

Fig. 2 Physical mechanisms and associated modeling framework of bubble formation around plasmonic nanoparticles. (a) Illustration of the different energy transfer mechanisms that span from the plasmon excitation to the generation of a nanoscale bubble. Their approximate timescales are indicated on the left axis. (b) Multiscale modeling framework used to describe these mechanisms. The individual blocks represent the three sub-models described in the text.

and convection are much slower than plasma relaxation, our model deals with these two channels separately. The initial volume of the bubble V_c is therefore defined as the volume of water heated above $0.9T_c$ by the plasma relaxation, combined to the volume of water-shell of thickness h_T that participates in the heat transfer at the water–metal interface. The $0.9T_c$ value corresponds to the spinodal temperature and has been shown both experimentally and numerically to drive the water molecules toward explosive phase change and spinodal decomposition.[26,27,32–36] Similarly, the initial bubble energy, water density and bubble-wall velocity after the shockwave emission are each evaluated by considering separately these two energy transfer channels. A more detailed description can be found in the Methods section and in ESI II.†

Finally, the bubble dynamics sub-model (Sub-Model III) simulates the temporal evolution of the bubble radius, wall velocity and energy after the shockwave emission using a cavitation model based on the Gilmore equation,[37] a weakly compressible generalization of the Rayleigh–Plesset model known for its accuracy even at large bubble wall velocities.[38] Our bubble dynamic model complements Gilmore's with additional mass and heat transfer equations at the bubble wall, based on the work of Kreider *et al.*[39] and a temperature and density dependent enthalpy (ESI III†). The bubble lifetime typically spans 0.1–100 ns, although longer lifetimes may occur for very large bubbles.

Many of the parameters from the bubble cavitation and dynamics sub-models are not precisely known at the temperatures and pressures relevant to plasmon-enhanced nanocavitation, but are nevertheless required for quantitative predictions of the bubble behavior. These unknown parameters are summarized in Fig. 3b and c. From the cavitation sub-model, these include the thickness h_T of the conduction water shell and two parameters that define the functional form of the energy lost

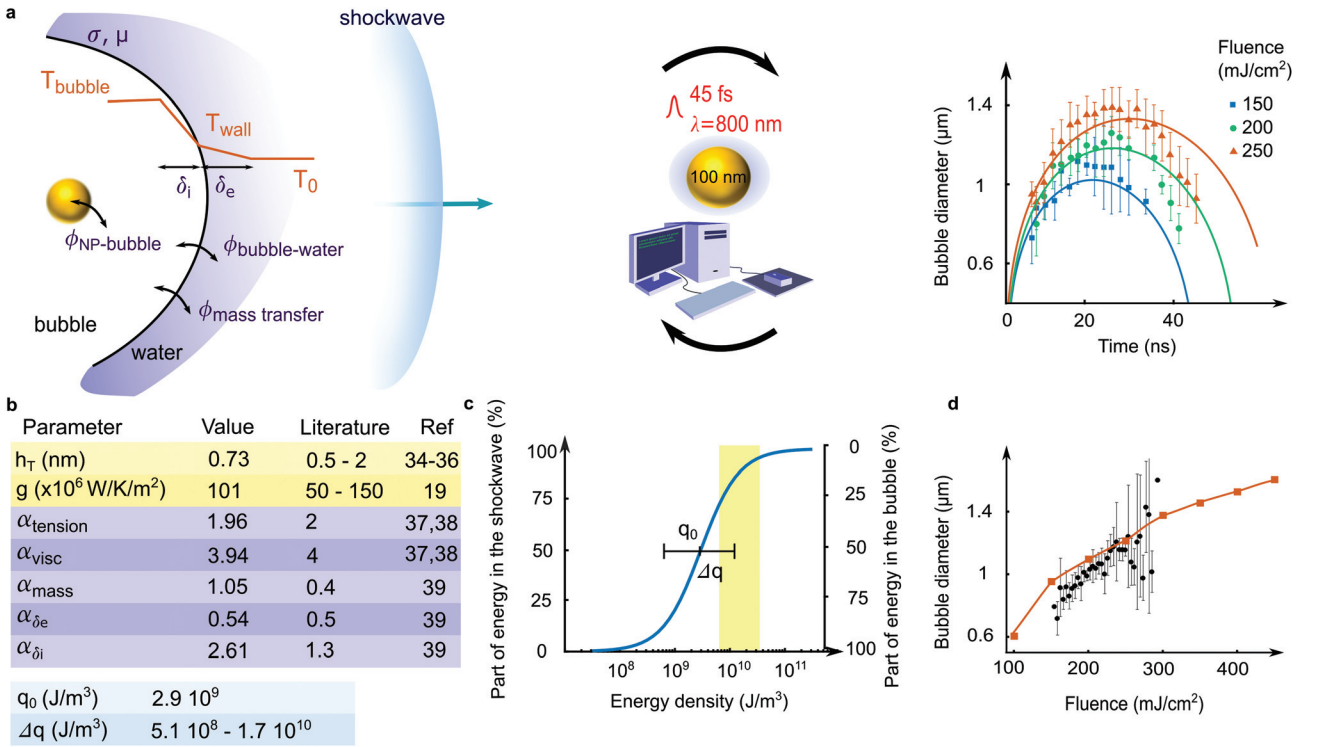

Parameter	Value	Literature	Ref
h_T (nm)	0.73	0.5 - 2	34-36
g (x10^6 W/K/m^2)	101	50 - 150	19
$\alpha_{tension}$	1.96	2	37,38
α_{visc}	3.94	4	37,38
α_{mass}	1.05	0.4	39
$\alpha_{\delta e}$	0.54	0.5	39
$\alpha_{\delta i}$	2.61	1.3	39
q_0 (J/m^3)	2.9 10^9		
Δq (J/m^3)	5.1 10^8 - 1.7 10^{10}		

Fig. 3 Parameterization of the modeling framework using a machine-learning strategy. (a) From left to right: the cavitation and bubble dynamics model contains a series of unknown parameters that must be determined to yield accurate prediction of bubble dynamics. The values of the parameters are numerically optimized *via* comparison of the bubble dynamics predictions for 45 fs, 800 nm irradiation of 100 nm AuNPs with experimental data from Boutopoulos *et al.*[30] Peak fluence is used. (b) Optimized parameter values obtained for the top-scoring solution. Values reported in the literature are indicated when available. (c) Portion of the energy that dissipates in the shockwave as a function of the bubble energy density. Highlighted is the range of energy densities corresponding to the points shown in (d). (d) Prediction of the bubble size after 20 ns for the same laser wavelength and pulse width, and comparison with experimental data from Boutopoulos *et al.*[30] The *x* axis is peak fluence.

to the initial shockwave (q_0 and Δq). Parameters from the bubble dynamics sub-model include the thermal conductivity g at the particle–vapor interface, the heat ($\alpha_{\delta e}$, $\alpha_{\delta i}$) and mass (α_{mass}) transfer at the bubble wall, as well as the viscous and surface tension (α_{visc} and $\alpha_{tension}$).

The precise evaluation of these nine mechanical and thermodynamical parameters from first-principles is extremely challenging. Instead, we chose to optimize their values by training the cavitation and bubble dynamics model on an experimental dataset of plasmon-induced bubble dynamics previously published by Boutopoulos *et al.*[30] (see Methods). These data include the transient diameters of bubbles generated around single 100 nm AuNPs irradiated with a single 800 nm, 45 fs, linearly polarized laser pulse at three different peak fluences (150, 200, and 250 mJ cm^{-2}), characterized with the shadowgraphic imaging technique (Fig. 3a). Using a global optimization scheme, the parameters were optimized to reduce the deviation between the simulated and the experimental bubble dynamics, yielding a final deviation of ≃0.4 times the experimental standard deviation (Fig. 3a). As shown in Fig. 3b, parameters from the top-scoring solution are very similar to some of the values reported in the literature for similar systems.

As a first test of the capability of our modeling framework, we sought to predict the diameters of bubbles produced at laser fluences that slightly differ from the ones on which it was trained. This new dataset, also from Boutopoulos *et al.*,[30] along with the simulated diameters are presented in Fig. 3d. The results show that our modeling framework could estimate these bubble diameters with an average error inferior to the experimental uncertainty of 150 nm. This is an early demonstration that our model can be applied to data outside of the optimization dataset.

To further assess the performance of our multiscale nanocavitation modeling framework, we tested its predictions against various experimental datasets available in the literature[18] as well as new data from extensive shadowgraph imaging and time-resolved spectroscopy that we performed to validate our framework. Specific irradiation condition and nanostructures were chosen in order to represent the state-of-the-art of *in vivo* and *in vitro* research for cell nanosurgery and laser-based tumor treatment.

First, we employed our modeling framework to investigate nanocavitation near the plasmonic resonance, which is representative of the most current plasmon-based cell nanosurgery. We thus simulated the cavitation around 9 nm AuNPs,

irradiated with 400 nm, 100 fs laser pulses for laser peak fluences up to 150 mJ cm^{-2}. At this wavelength, the resistive losses within the NPs are very strong, and energy deposition inside the NP dominates near-field plasma generation. We compared our simulated bubble dynamics and maximal diameters with experimental data previously published by Kotaidis and Plech,[18] reported in Fig. 4a and b together with our predictions. These are in very good agreement with all experimental data, with an average deviation of less than 2 nm, below the experimental error, despite the fact that bubbles generated by this system are much smaller than the one on which the model was initially optimized (radius of 20 nm *vs.* 500 nm). The mechanism by which the bubble is formed is also completely different, being mostly plasma-mediated for the training set (30–98% of the energy is deposited in the plasma), and completely NP-mediated for this system (>80% of the energy is deposited in the particle by resistive losses, even more at low fluences).

Then, we sought to study the effect of both particle diameter and pulse duration on the bubble size. Note that the

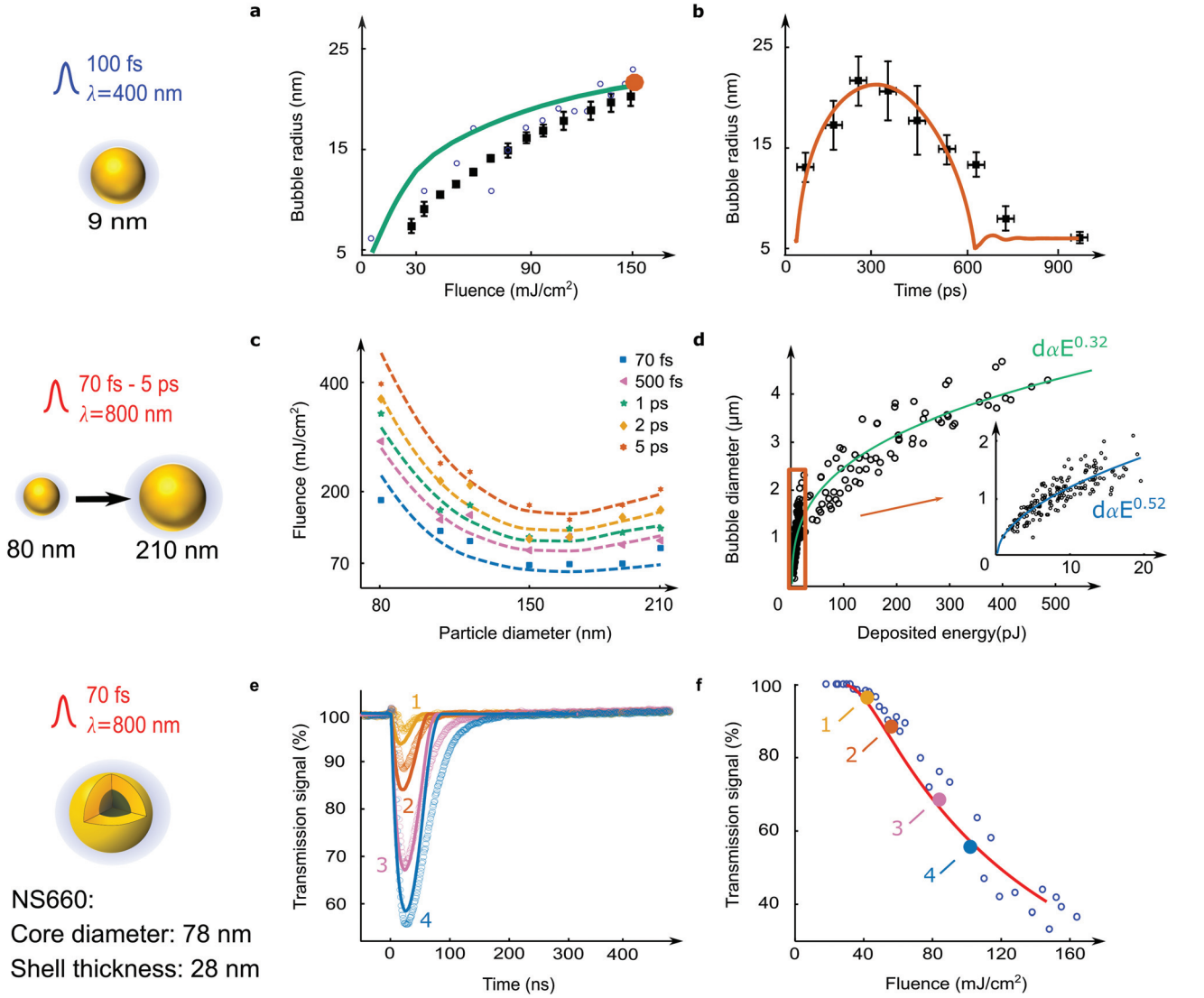

Fig. 4 Predictions of our modeling framework for various NP shapes, sizes and irradiation parameters. (a) Prediction of the maximal radius and (b) dynamics for a 9 nm AuNP irradiated with 100 fs, 400 nm laser pulses. Dynamics is shown at a peak fluence of 150 mJ cm^{-2}. The experimental values are taken from Kotaidis and Plech.[18] The black squares and blue circles show values obtained with the SAXS and the liquid scattering methods, respectively. (c) Time-resolved shadowgraphic imaging characterization of the cavitation threshold around NPs of various sizes irradiated with 800 nm laser pulses of various pulse widths. Dotted lines show the predicted fluence required to generate bubbles with a diameter of 1.04 μm that best fits the data. (d) Maximal bubble diameters obtained for numerous pulse widths, particle diameters and fluences. A $d\alpha E^{1/3}$ law accurately describes the behavior for large bubbles. The inset focuses on smaller bubbles, for which a different $d\alpha E^{1/2}$ law is deduced. (e) Probe scattering signal acquired (circle) and simulated (lines) for cavitation around a NS660 AuNS irradiated with 70 fs, 800 nm laser pulses at various fluences (42, 56, 84 and 102 mJ cm^{-2}). (f) Experimental (circle) and simulated (line) evolution of the minimum level of the transmission signal as a function of the incident average laser fluence.

experimental setup cannot reliably detect bubbles of diameters smaller than about the probe laser wavelength. The actual bubble formation threshold is therefore lower than what we can measure experimentally, which we define as the visibility threshold, which corresponds in our case to bubbles with diameters of ≃0.8–1 μm. We experimentally determined the visibility threshold for an extended library of AuNPs with diameters between 80 and 210 nm, irradiated with 800 nm laser pulses of time width ranging from 70 fs to 5 ps. We synthesized the AuNP solutions using a seeded growth approach, see Methods for additional information. We then characterized the experimental cavitation thresholds for all these particles with the time-resolved shadowgraphic imaging technique that allows for individual bubbles observation (see Methods). Experimental results are reported in Fig. 4c (the numerical values can be found in ESI V†), each point representing the highest fluence at which no bubble could be detected, corresponding to bubbles with diameters of ≃0.8–1 μm. The simulation results are shown in the same panel, the thick, dotted lines indicating the laser fluence required to generate bubbles with a maximal diameter of 1.04 μm for each AuNP and laser pulse width. This diameter was determined by minimizing the deviation with the experimental results, and is in very good agreement with the expected limit of detection of our shadowgraphic system. Interestingly, the simulated bubble diameters seem to generally follow a power-law relative to the calculated deposited energy (E_{dep}) (Fig. 4d). For bubbles larger than ≃1.5 μm (E_{dep} > 20 pJ), the bubble diameters follow the general rule $d \alpha {E_{dep}}^{0.32}$, which was expected since the energy of a bubble is commonly assumed to be equal to the work of pressure $E_{bubble} = (p_{water} - p_{bubble}) \times V_{bubble}$. However, for smaller bubbles (E_{dep} < 20 pJ), the energy coefficient is increased to $d \alpha {E_{dep}}^{0.52}$, as observed experimentally by Siems *et al.*,[19] indicating the increased influence of the surface for very small bubbles. Using our model, we could further identify that this peculiar hydrodynamic effect was a direct consequence of the increased contributions of the surface tension and water viscosity on small bubble dynamics (ESI VI†).

Finally, we sought to predict cavitation induced from other geometries of plasmonic nanostructures beside homogeneous spheres. We chose to tackle cavitation around AuNS with a core diameter and shell thickness of 78 nm and 28 nm, respectively, when irradiated at 800 nm with a 70 fs laser pulse. Previous identification of this AuNS as being optimal for cavitation under this particular irradiation parameter motivated our choice.[6] Using the scattering imaging technique (Methods), we measured the bubble dynamics around these AuNS at several average fluences between 10 mJ cm^{-2} and 170 mJ cm^{-2}. The time-resolved transmissions of the probe signals are reported in Fig. 4e. We then used our modeling framework to calculate the predicted bubble dynamics and used the Mie theory and a Gaussian beam assumption to calculate the associated probe extinction signal. Simulation results are in very close agreement with the experimental data (Fig. 4e), and reproduce the asymmetry of the growth and collapse phases observed at lower fluences (ESI VII†). The early disappearance of the smaller bubbles located far from the focal plane has been identified as the source of this asymmetry. At a larger fluence, our model does not capture the observed slower collapse, probably because it originates from bubble rebounds that are not accurately described by our framework, since this behavior was completely absent from the training dataset. Despite this, the maximal signal transmission as a function of fluence could be predicted with a relatively high accuracy (Fig. 4f).

The very good agreement between the predicted and observed bubbles for these three systems suggests that the developed modeling framework can be reliably used to quantitatively predict the cavitation dynamics and threshold around plasmonic nanoparticles with various shapes, materials and irradiation conditions, providing a valuable tool for designing nanomaterials for bubble-based *in vivo* and *in vitro* treatments. In addition to being particularly accurate, full bubble dynamics calculations can be made rather rapidly, a typical calculation taking between 6 h and 15 h on a standard personal desktop computer, which makes the model particularly well adapted for prototyping.

Another important aspect of our model is that it uniquely enables characterizing critical physical parameters of the laser–particle interaction that would be difficult to observe otherwise. For instance, using the simulation data presented in Fig. 4c, we investigated the cavitation volume, energy deposition, as well as the plasma density and temperature for AuNPs of diameters 80–210 nm irradiated with 800 nm laser pulses with a pulse width of 70 fs–5 ps at a fluence corresponding to their observed cavitation threshold (diameter of ≃1 μm). Interestingly, the initial bubble volume is almost unique due to the plasma relaxation for all diameters and pulse width tested, the contribution from heat conduction at the NP interface being marginal in all cases (Fig. 5a). This indicates that a plasma-mediated mechanism generally dominates cavitation for AuNPs irradiated with femtosecond and picosecond pulses at 800 nm, irrespective of their size. However, the energy that needs to be deposited to initiate cavitation is highly dependent on the size and pulse width, higher energy being required for small particles at short pulses, and for large particles at longer pulses (Fig. 5b). This behavior results from the combination of two competing phenomena. First, the preferential plasmon energy decay channel is shown to switch from plasma relaxation to conduction at the NP interface as the pulse width and NP diameters are increased (Fig. 5c). Cavitation is thus favored for smaller NPs and shorter pulses. Second, the initial cavitation bubble is shown to be much smaller for small NPs (Fig. 5d). The contribution of the bubble surface tension to the bubble growth is thus much more important for smaller NPs, which reduces their cavitation efficiency. The energy lost by the bubble to the initial shockwave is also much more important for smaller NPs, probably due to the increased stress confinement (Fig. 5e). These phenomena thus explain the peculiar behavior observed in Fig. 5b. Importantly, cavitation is shown to occur when a deposited energy density of ≃1.7×10^9 J m^{-3} is reached inside

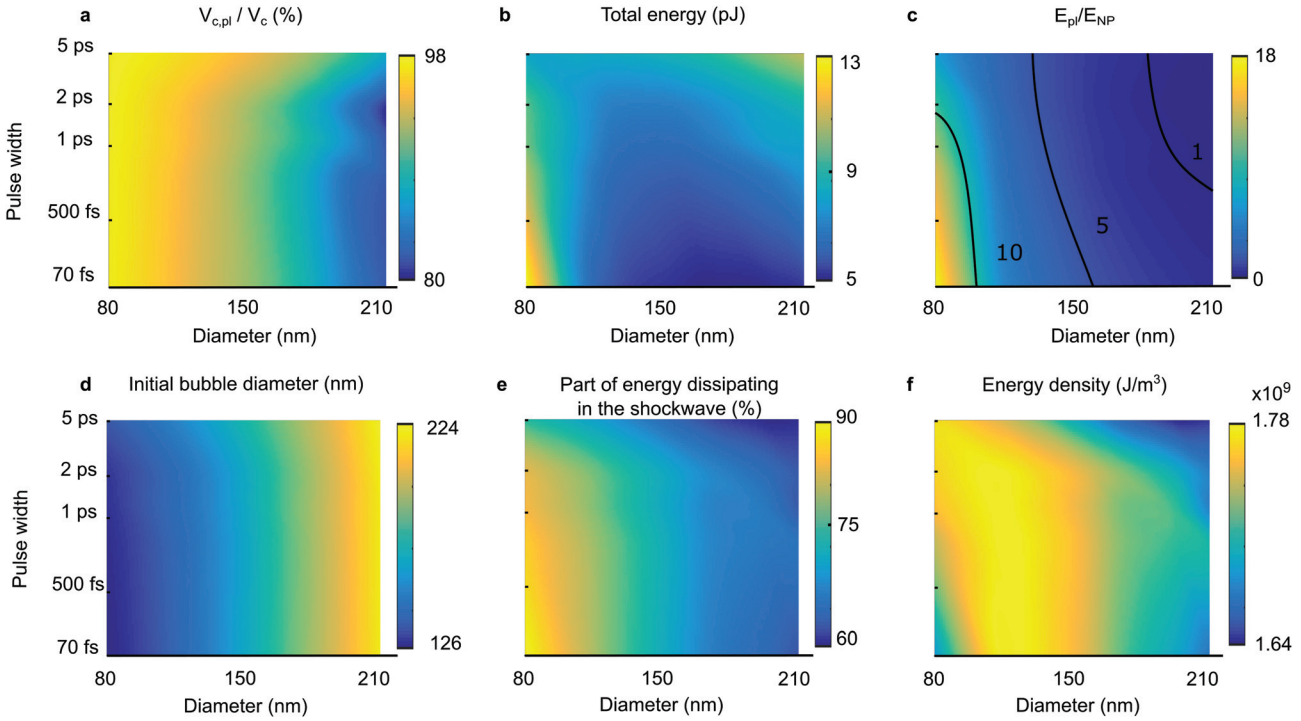

Fig. 5 Plasma calculations from the 3D model step in Fig. 4c at the cavitation threshold. (a) Contribution of the plasma-heated volume $V_{c,pl}$ to total the initial bubble volume V_c. (b) Total energy deposited in the plasma and in the NP. (c) Ratio of the energy absorbed in the plasma and in the NP. (d) Initial bubble diameter corresponding to V_c. (e) Portion of the deposited energy that is dissipated in the shockwave. (f) Energy density in the initial bubble of volume V_c.

the initial bubble, irrespective of the NP diameter and pulse width (Fig. 5f), which corresponds to the energy density necessary to isochorically heat water of ≃400 K, close to the spinodal temperature. Reaching a critical electronic plasma density of 10^{21} cm^{-3}, a criterion usually used to predict laser-induced cavitation, seems however inadequate for plasmon-enhanced cavitation (ESI VIII†), which makes our modeling framework essential for the reliable prototyping of nanomaterials specifically designed for nanobubble-based applications.

Conclusions

In summary, we have presented a multiscale modeling framework able to predict, for the first time, the dynamics and formation threshold of bubbles generated around plasmonic nanostructures in water from first principles. This framework couples a 3D finite-element based model of energy deposition, including non-linear photoexcitation of a plasma in the near-field, with a cavitation and a bubble dynamic model, and allows for the rapid calculation required for the development of a tool that can be used for efficient prototyping. Our results have shown that the framework is generalizable to a large class of nanostructure size, shapes and irradiation regimes, offering an unprecedented capability for the computational design of non-linear plasmonic nanomaterials for nanocavitation. Further testing could be carried out, by investigating other metals besides gold and various polarizations, as well as longer pulse widths, for which models already exist.[40,41] In the future, this framework could be used to screen large libraries of plasmonic nanostructure shapes, sizes and materials for the design of plasmonic nanodevices with enhanced properties.[14,25] Following recent advances in bottom-up assemblies of complex plasmonic structures,[42–44] we also envision using this methodology for the computational design of complex materials specifically tailored to enhance cavitation and other non-linear plasmon-enhanced interactions, and optimize experimental settings for *in vivo* studies.[9,10,45] New customized materials and devices with programmable properties should boost the development of new plasmon-based therapeutics and biosensing approaches in the field of nanomedicine.

Methods

Sample preparation

AuNP solutions were prepared using a seeded growth approach, resulting in the final atomic gold and citrate concentration of 300 μM and 2 mM, respectively. UV-visible-NIR absorption spectra were acquired for each solution with an Epoch microplate spectrophotometer and analyzed to precisely evaluate the AuNP size based on Mie theory. The working

AuNP solutions were all diluted to a final concentration of 1.7×10^8 NP per mL using ddH_2O.

AuNS solution (a silica core diameter of 78 nm with a shell thickness of 28 nm) was provided by NanoComposix Inc., with citrate conjugation. These particles were dispersed in water with a concentration of 2.7×10^9 NS per mL and their plasmonic resonance peak was located at 660 nm. This solution has been transferred into a 1×1 cm^2 quartz cuvette without any dilution for time-resolved probe scattering measurements.

Time-resolved shadowgraphic imaging

AuNP samples were prepared by adding 30 μL of solution in a glass bottom Petri dish (MatTek), which was then sealed with a cover slip to form a ≃0.05 cm^3 microcontainer. Laser excitation was carried out using a Ti:sapphire laser (800 nm, a tunable pulse width 70 fs to 5 ps, 10 Hz repetition rate, Spitfire, Spectra-Physics). Bubble detection was performed using a 6 ns broadband probe pulse resulting from the fluorescence emission of a laser (Nd:YAG, 532 nm, 6 ns, 10 Hz, Brilliant B, Quantel) excited rhodamine dye and co-aligned with the pump beam. Individual nanobubbles can be continuously tracked in time and space since the data acquisition rate (10 Hz) is faster than the AuNP Brownian motion (≃1 s to exit the field of view). Readers are referred to previously published work for more details.[6,30] The experimental cavitation threshold was determined as the minimum laser fluence resulting in repeatable bubble formation around a single AuNP at 5 ns pump–probe delay.

Time-resolved probe scattering

A pump laser beam (Ti:sapphire, 800 nm, 70 fs, 10 Hz, Spitfire, Spectra-Physics) was co-aligned with a probe laser beam (He : Ne, 633 nm, 2 mW, continuous-wave, Thorlabs). The probe is spatially filtered with a 10 μm pinhole after passing through the sample. The probe scattering signal intensity was measured with a 2 GHz high-speed photodetector (SV2-FC, free space, Thorlabs). Further details can be found in ref. 6 and 31.

Modeling framework

Energy deposition sub-model. The electromagnetic field distribution (**E**,**H**) is calculated with the Helmholtz equation at every time-step. Ionization in the near-field is computed using the strong field formalism of Keldysh[46] that includes multiphoton and tunnel ionization, water being assumed to behave as a 6.5 eV gap amorphous semiconductor.[26] Impact ionization is described with a dense plasma theory formalism.[47,48] The plasma density and energy time-dependent distribution are calculated with a semiclassical Boltzmann transport formalism. The presence of plasma in the near-field locally modifies the dielectric function using a Drude formalism. For strong enough modifications of the local permittivity, the linear relationship between fluence and energy absorption of the NP is lost. Moreover, the pulse duration being shorter than the electron–phonon relaxation time, the electrons and lattice are heated out of equilibrium. This effect is particularly important in the first few tens of ps, which are crucial for the onset of bubble nucleation. A parabolic two-temperature model is therefore used to adequately capture heat transfer at these time scales and precisely calculate the electron and lattice temperatures inside the NP.[3,49] The modification of the NP's optical properties due to the excitation of hot electrons during the laser pulse[50] is neglected (see ESI I†). The water temperature is calculated with the heat equation, including contribution from the plasma relaxation[3,26] and heat conduction at the interface with the nanoparticle.[24] Water heating is assumed to be isochoric. The complete sub-model consists of 6 partial differential equations (PDE) solved in 3D with the finite elements software Comsol (Comsol, Inc., Burlington), in a domain of radius corresponding to the irradiation wavelength. Perfectly matched layers were used. Complete geometry tallies up to ≃45 000 tetrahedral second order elements. A generalized-α solver with Comsol's default settings was used for time-stepping. Readers are referred to ESI I† for additional details.

Cavitation sub-model. The initial volume of the bubble is calculated as the sum of the two volumes heated respectively by plasma relaxation and conduction. A volume $V_{c,pl}$ is calculated as the volume of water reaching a temperature above $0.9T_c$ [32,33] at the end of the energy deposition sub-model. The density ($\rho_{c,pl}$) and temperature ($T_{c,pl}$) for this layer are calculated assuming an isochoric transition. The temperature of a water shell of thickness h_T is calculated using a 0D two-temperature model completed with an entropy rate equation written for the water shell. The set of ordinary differential equations (ODEs) is solved with the Matlab ode45 solver. The density ($\rho_{c,NP}$) and temperature ($T_{c,NP}$) of this layer are extracted from the computed entropy, assuming that the volume is heated along the binodal. The corresponding volume $V_{c,NP}$ is added to $V_{c,pl}$ to yield V_c. The shockwave velocity and then the velocity of particles in the wake of the shockwave are calculated with the Rankine–Hugoniot relationships, the latter velocity being approximated as the initial bubble wall velocity. A weighted average from the velocities calculated separately from the two pressures in the two volumes $p_{c,pl}$ and $p_{c,NP}$ was used. Readers are referred to ESI II† for additional details.

Bubble dynamics sub-model. The bubble dynamics sub-model yields the temporal evolution of the bubble diameter, energy and particle temperature. A Gilmore-like model[37] that generalizes the Rayleigh–Plesset equation by including weak compressibility effects is completed with an energy conservation equation and heat and mass fluxes at the bubble wall as well as heat transfer at the vapor–particle interface, adapted from a previous model from Kreider *et al.*[39] Ballistic thermal flux from the particle to the surrounding water,[41] although probably critical for bubbles with many rebounds and for ns laser irradiation, is not relevant in our case. These ODEs were solved with the Backward Differentiation Formula (BDF) solver implemented in the COMSOL software. The readers are referred to ESI III† for additional details.

Parameters optimization. The NLopt implementation (http://ab-initio.mit.edu/nlopt) of the COBYLA gradient-free optimizer

was used to optimize our 9 parameters, based on the minimization of the sum of squared residual relative to the experimental data. This procedure was performed in parallel from 40 randomly selected distinct starting points in the search space. Every 50 000 iterations, the search space was reduced, based on the optimal parameters of the top 100 solutions. The readers are referred to ESI V† for additional details.

Acknowledgements

Yves Drolet is acknowledged for technical support and David Rioux for synthesizing most of the nanoparticles used for this article. The authors thank the Natural Science and Engineering Research Council (NSERC) and Le Fond Québecois de la Recherche sur la Nature et les Technologies (FQRNT) for financial support. C. B. acknowledges funding from the EU under a Marie Curie Fellowship, FP7-PEOPLE-2013-IOF, project reference 624888.

Notes and references

1 J. A. Schuller, E. S. Barnard, W. Cai, Y. C. Jun, J. S. White and M. L. Brongersma, *Nat. Mater.*, 2010, **9**, 193–204.
2 M. Kauranen and A. V. Zayats, *Nat. Photonics*, 2012, **6**, 737–748.
3 É. Boulais, R. Lachaine and M. Meunier, *Nano Lett.*, 2012, **12**, 4763–4769.
4 K. K. Ostrikov, F. Beg and A. Ng, *Rev. Mod. Phys.*, 2016, **88**, 011001.
5 É. Boulais, R. Lachaine, A. Hatef and M. Meunier, *J. Photochem. Photobiol., C*, 2013, **17**, 26–49.
6 R. Lachaine, C. Boutopoulos, P.-Y. Lajoie, É. Boulais and M. Meunier, *Nano Lett.*, 2016, **16**, 3187–3194.
7 D. O. Lapotko, E. Y. Lukianova-Hleb and A. A. Oraevsky, *Lasers Surg. Med.*, 2006, **38**, 631–642.
8 A. Csaki, F. Garwe, A. Steinbrück, G. Maubach, G. Festag, A. Weise, I. Riemann, K. König and W. Fritzsche, *Nano Lett.*, 2007, **7**, 247–253.
9 E. Y. Lukianova-Hleb, Y.-S. Kim, I. Belatsarkouski, A. M. Gillenwater, B. E. O'Neill and D. O. Lapotko, *Nat. Nanotechnol.*, 2016, **11**, 525–532.
10 P. Chakravarty, W. Qian, M. A. El-Sayed and M. R. Prausnitz, *Nat. Nanotechnol.*, 2010, **5**, 607–611.
11 A. Schroeder, D. A. Heller, M. M. Winslow, J. E. Dahlman, G. W. Pratt, R. Langer, T. Jacks and D. G. Anderson, *Nat. Rev. Cancer*, 2011, **12**, 39–50.
12 M. Schomaker, D. Heinemann, S. Kalies, S. Willenbrock, S. Wagner, I. Nolte, T. Ripken, H. Escobar, H. Meyer and A. Heisterkamp, *J. Nanobiotechnol.*, 2015, **13**, 10.
13 J. Baumgart, L. Humbert, É. Boulais, R. Lachaine, J. J. Lebrun and M. Meunier, *Biomaterials*, 2012, **33**, 2345–2350.
14 M. S. Yavuz, Y. Cheng, J. Chen, C. M. Cobley, Q. Zhang, M. Rycenga, J. Xie, C. Kim, K. H. Song, A. G. Schwartz, L. V. Wang and Y. Xia, *Nat. Mater.*, 2009, **8**, 935–939.
15 D. Peer, J. M. Karp, S. Hong, O. C. Farokhzad, R. Margalit and R. Langer, *Nat. Nanotechnol.*, 2007, **2**, 751–760.
16 É. Boulais, R. Lachaine and M. Meunier, *J. Phys. Chem. C*, 2013, **117**, 9386–9396.
17 G. De Fabritiis, R. Delgado-Buscalioni and P. V. Coveney, *Phys. Rev. Lett.*, 2006, **97**, 134501.
18 V. Kotaidis and A. Plech, *Appl. Phys. Lett.*, 2005, **87**, 1–3.
19 A. Siems, S. A. L. Weber, J. Boneberg and A. Plech, *New J. Phys.*, 2011, **13**, 22.
20 J. Lombard, T. Biben and S. Merabia, *Phys. Rev. Lett.*, 2014, **112**, 105701.
21 M. L. Brongersma, N. J. Halas and P. Nordlander, *Nat. Nanotechnol.*, 2015, **10**, 25–34.
22 M. I. Stockman, *Opt. Express*, 2011, **19**, 22029.
23 A. Manjavacas, J. G. Liu, V. Kulkarni and P. Nordlander, *ACS Nano*, 2014, **8**, 7630–7638.
24 O. Ekici, R. K. Harrison, N. J. Durr, D. S. Eversole, M. Lee and A. Ben-Yakar, *J. Phys. D: Appl. Phys.*, 2008, **41**, 185501.
25 L. Novotny and N. van Hulst, *Nat. Photonics*, 2011, **5**, 83–90.
26 A. Vogel, J. Noack, G. Hüttman and G. Paltauf, *Appl. Phys. B*, 2005, **81**, 1015–1047.
27 P. Lorazo, L. J. Lewis and M. Meunier, *Phys. Rev. Lett.*, 2003, **91**, 225502.
28 S. K. Sundaram and E. Mazur, *Nat. Mater.*, 2002, **1**, 217–224.
29 E. Y. Lukianova-Hleb, Y. Hu, L. Latterini, L. Tarpani, R. A. Drezek, J. H. Hafner and D. O. Lapotko, *ACS Nano*, 2010, **4**, 2109–2123.
30 C. Boutopoulos, A. Hatef, M. Fortin-Deschênes and M. Meunier, *Nanoscale*, 2015, **7**, 11758–11765.
31 R. Lachaine, É. Boulais and M. Meunier, *ACS Photonics*, 2014, **1**, 331–336.
32 V. Kotaidis, C. Dahmen, G. von Plessen, F. Springer and A. Plech, *J. Chem. Phys.*, 2006, **124**, 184702.
33 M. T. Carlson, A. J. Green and H. H. Richardson, *Nano Lett.*, 2012, **12**, 1534–1537.
34 K. Sasikumar and P. Keblinski, *J. Chem. Phys.*, 2014, **141**, 234508.
35 Y. Dou, L. V. Zhigilei, Z. Postawa, N. Winograd and B. J. Garrison, *Nucl. Instrum. Methods Phys. Res., Sect. B*, 2001, **180**, 105–111.
36 Y. Dou, L. V. Zhigilei, N. Winograd and B. J. Garrison, *J. Phys. Chem. A*, 2001, **105**, 2748–2755.
37 F. R. Gilmore, *The Growth or Collapse of a Spherical Bubble in a Viscous Compressible Liquid*, California institute of technology technical report, 1952.
38 A. Prosperetti and A. Lezzi, *J. Fluid Mech.*, 1986, **168**, 457–478.
39 W. Kreider, L. A. Crum, M. R. Bailey and O. A. Sapozhnikov, *J. Acoust. Soc. Am.*, 2011, **130**, 3511–3530.
40 E.-A. Brujan, *Appl. Mechanics*, 2013, **58**, 231–240.
41 J. Lombard, T. Biben and S. Merabia, *Nanoscale*, 2016, **8**, 14870–14876.

42 R. Schreiber, J. Do, E.-M. Roller, T. Zhang, V. J. Schüller, P. C. Nickels, J. Feldmann and T. Liedl, *Nat. Nanotechnol.*, 2013, **9**, 74–78.
43 W. Sun, É. Boulais, Y. Hakobyan, W. L. Wang, A. Guan, M. Bathe and P. Yin, *Science*, 2014, **346**, 1258361.
44 A. Kuzyk, R. Schreiber, H. Zhang, A. O. Govorov, T. Liedl and N. Liu, *Nat. Mater.*, 2014, **13**, 862–866.
45 E. Y. Lukianova-Hleb, X. Ren, R. R. Sawant, X. Wu, V. P. Torchilin and D. O. Lapotko, *Nat. Med.*, 2014, **20**, 778–784.
46 L. V. Keldysh, *J. Exp. Theor. Phys.*, 1965, **20**, 1307–1314.
47 N. E. Andreev, M. E. Veisman, V. P. Efremov and V. E. Fortov, *High Temp.*, 2003, **41**, 594–608.
48 L. Hallo, A. Bourgeade, V. T. Tikhonchuk, C. Mezel and J. Breil, *Phys. Rev. B: Condens. Matter Mater. Phys.*, 2007, **76**, 1–12.
49 J. K. Chen, D. Y. Tzou and J. E. Beraun, *Int. J. Heat Mass Transfer*, 2006, **49**, 307–316.
50 S. Link, C. Burda, Z. L. Wang and M. A. El-Sayed, *J. Chem. Phys.*, 1999, **111**, 1255.